



A Fast-growing Tilt Instability of Detached Circumplanetary Disks

Rebecca G. Martin¹ , Zhaohuan Zhu¹ , and Philip J. Armitage^{2,3} ¹Department of Physics and Astronomy, University of Nevada, Las Vegas, 4505 South Maryland Parkway, Las Vegas, NV 89154, USA²Center for Computational Astrophysics, Flatiron Institute, New York, NY 10010, USA³Department of Physics and Astronomy, Stony Brook University, Stony Brook, NY 11794, USA

Received 2020 May 30; revised 2020 July 4; accepted 2020 July 8; published 2020 July 24

Abstract

Accretion disks in binary systems can exhibit a tilt instability, arising from the interaction between components of the tidal potential and dissipation. Using a linear analysis, we show that the aspect ratios and outer radii of circumplanetary disks provide favorable conditions for tilt growth. We quantify the growth rate of the instability using particle-based (PHANTOM) and grid-based (ATHENA++) hydrodynamic simulations. For a disk with outer aspect ratio $H/r \simeq 0.1$, initially moderate tilts double on a timescale of about 15–30 binary orbits. Our results imply that detached circumplanetary disks, whose evolution is not entirely controlled by accretion from the circumstellar disk, may commonly be misaligned to the planetary orbital plane. We discuss implications for planetary spin evolution, and possible interactions between the tilt instability and Kozai–Lidov dynamics.

Unified Astronomy Thesaurus concepts: [Stellar accretion disks \(1579\)](#); [Planet formation \(1241\)](#); [Protoplanetary disks \(1300\)](#); [Exoplanet formation \(492\)](#); [Planetary theory \(1258\)](#); [Satellite formation \(1425\)](#); [Circumstellar disks \(235\)](#); [Hydrodynamics \(1963\)](#); [Pre-main sequence stars \(1290\)](#); [Disk galaxies \(391\)](#); [Planetary system formation \(1257\)](#); [Solar system planets \(1260\)](#)

1. Introduction

A forming planet is able to tidally open a gap in the protoplanetary disk once its mass roughly exceeds that of Neptune (Lin & Papaloizou 1986; D’Angelo et al. 2002; Bate et al. 2003). Material continues to flow into the gap (Artymowicz & Lubow 1996). Since the size of the planet is much smaller than the Hill radius, a circumplanetary disk forms (Lubow et al. 1999; D’Angelo et al. 2002). Most of the mass of gas giants such as Jupiter may have been accreted from their circumplanetary disks and thus the orientation of the disk has a significant impact on the forming planet. Circumplanetary disks are also the birthplace of regular satellites (those with low orbital inclination to the equatorial plane of the planet and low orbital eccentricities; Lunine & Stevenson 1982; Canup & Ward 2002; Mosqueira & Estrada 2003; Batygin & Morbidelli 2020), and may provide some of the most prominent observational signatures of forming planets (Zhu 2015).

Motivation for considering the possibility of misaligned circumplanetary disks comes from planetary obliquities, which are large for Saturn, Uranus, and Neptune. The regular satellites and ring systems of these planets are close to being aligned with the spin. A variety of late-time processes can produce planet spin–orbit misalignment, including giant impacts (Safronov 1966; Benz et al. 1989; Morbidelli et al. 2012), spin–orbit resonances (Ward & Hamilton 2004; Brasser & Lee 2015; Vokrouhlický & Nesvorný 2015; Rogoszinski & Hamilton 2020), and planet–circumstellar disk interactions (especially for planets at smaller orbital separation; Millholland & Batygin 2019). A primordial contribution, however, is also of interest. In extrasolar planetary systems, misaligned circumplanetary disks or ring systems would have deep transit signatures. This has led to suggestions that some very low density planets (Jontof-Hutter et al. 2014; Masuda 2014) might be reinterpreted as planets with misaligned disks or rings (Piro & Vissapragada 2020; Akincanmi et al. 2020).

Small misalignments between the planetary orbital plane and that of the circumplanetary disk could arise from the

stochastic accretion of gas from a turbulent protoplanetary disk (Gressel et al. 2013). Our goal in the Letter is to determine the conditions under which a small tilt might grow. Tilt instabilities in tidally distorted disks were first discovered by Lubow (1992). We make one key simplification: on the timescales of interest accretion onto the circumplanetary disk (studied for example by Tanigawa et al. 2012; Szulágyi et al. 2014; Schulik et al. 2020) can be neglected. In this “detached” limit, the dynamics of a misaligned disk are determined by two components of the tidal potential. The $m = 0$ component produces retrograde nodal precession of the disk. The disk is able to hold itself together through wave-like communication and precess as a solid body (Papaloizou & Terquem 1995; Larwood et al. 1996; Terquem 1998). The $m = 2$ component produces an “oscillating” torque with a period of half the orbital period, which does not affect the mean precession rate (Katz et al. 1982). In the presence of dissipation the $m = 0$ component leads to coplanar alignment, while the $m = 2$ term leads to the tilt increasing (Lubow 1992; Bate et al. 2000; Lubow & Ogilvie 2000). For circumstellar disks, typically the outcome is coplanar alignment. However, since circumplanetary disks are small and have a large disk aspect ratio, we show here that their tilt tends to increase. In Section 2 we use analytic methods to examine the behavior, while in Section 3 we use hydrodynamic simulations. We conclude in Section 4.

2. Analytic Estimates

We consider a planet of mass M_p orbiting a star of mass M_s at orbital separation a_p with orbital period $P_{\text{orb}} = 2\pi/\Omega_b$ where the orbital frequency is $\Omega_b = \sqrt{G(M_p + M_s)/a_p^3}$. Material in the circumplanetary disk at radius r orbits around the planet with Keplerian angular frequency $\Omega = \sqrt{GM_p/r^3}$. We consider properties of the disk.

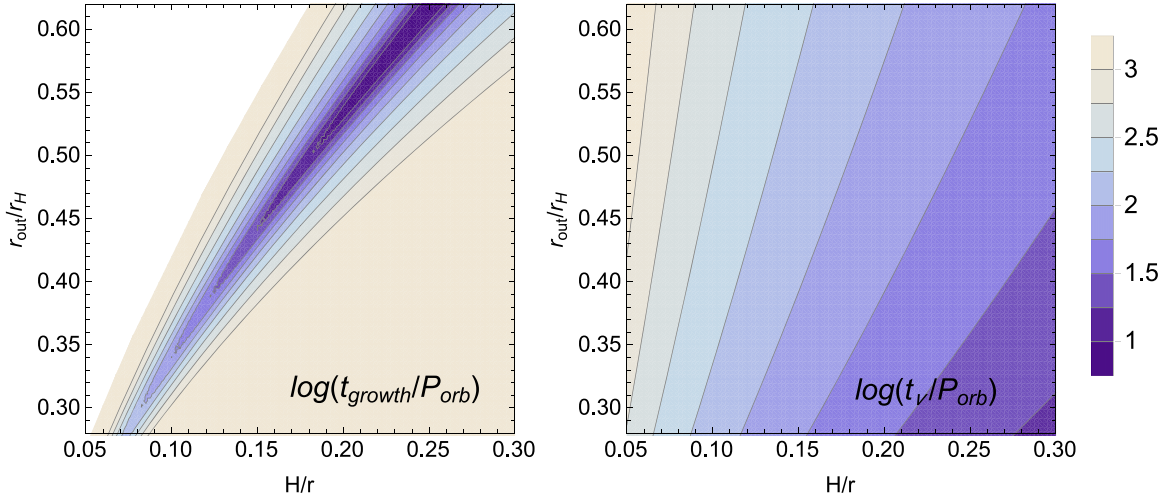


Figure 1. Left: contour plot of the log of the growth timescale of the tilt of a circumplanetary disk in units of the binary orbital period as a function of the disk aspect ratio H/r and the disk outer radius, r_{out} , in units of the Hill sphere radius. The planet mass is $M_p = 0.001 M_s$. The surface density is fixed as $\Sigma \propto r^{-3/2}$ distributed between $r_{\text{in}} = 0.03 r_H$ up to r_{out} . The disk viscosity is $\alpha = 0.01$. In the white region the disk tilt decreases. In the colored regions the disk tilt increases. Right: contour plot of the log of the disk viscous timescale in units of the binary orbital period.

2.1. Size of the Disk

The size of a circumplanetary disk is determined by tidal truncation effects due to the star (Paczynski 1977; D’Angelo et al. 2002; Ayliffe & Bate 2009a). A coplanar circumplanetary disk is initially truncated at a radius of about $r_{\text{out}} = 0.4 r_H$ (Martin & Lubow 2011), where the Hill sphere radius

$$r_H = a_p \left(\frac{M_p}{3M_s} \right)^{1/3}. \quad (1)$$

For typical parameters the Hill sphere radius is

$$r_H = 0.36 \left(\frac{a_p}{5.2 \text{ au}} \right) \left(\frac{M_p}{10^{-3} M_s} \right)^{1/3} \text{ au}. \quad (2)$$

The Hill sphere and therefore the disk size scale with the orbital semimajor axis of the planet. We note that the tidal truncation radius of a misaligned circumplanetary disk is larger than that of a coplanar disk (Lubow et al. 2015; Miranda & Lai 2015).

2.2. Viscous Evolution Timescale

The viscosity of the disk is

$$\nu = \alpha c_s H = \alpha \left(\frac{H}{r} \right)^2 r^2 \Omega, \quad (3)$$

where α is the Shakura & Sunyaev (1973) viscosity parameter, c_s is the disk sound speed, and H/r is the disk aspect ratio. The density of the disk falls off exponentially away from the midplane $\rho \propto \exp[-(1/2)(z/H)^2]$ (Pringle 1981), where H is the disk scale height. The disk aspect ratio of a circumplanetary disk can be significantly larger than that of a circumstellar disk with typical values in the range 0.1–0.3 (Ayliffe & Bate 2009b; Martin & Lubow 2011). The viscous timescale at the outer edge of the disk is

$$t_\nu = \frac{r_{\text{out}}^2}{\nu(r_{\text{out}})}, \quad (4)$$

which for our typical parameters is

$$\frac{t_\nu}{P_{\text{orb}}} = 232 \left(\frac{\alpha}{0.01} \right)^{-1} \left(\frac{H/r}{0.1} \right)^{-2} \left(\frac{r_{\text{out}}}{0.4 r_H} \right)^{3/2}. \quad (5)$$

This viscous timescale is shown as a function of H/r and the disk outer radius in the right panel of Figure 1 for $\alpha = 0.01$. The viscous timescale is a measure of the lifetime of the disk if there is no further accretion on to it. We do not include accretion on to the disk in our analysis of the evolution of the tilt of the disk. Accretion that occurs at close to zero inclination will act to lower the tilt of the disk.

2.3. Tilt Evolution of the Disk

The angular momentum of each ring of the disk with surface density $\Sigma(r)$ is defined by the complex variable $W = l_x + il_y$, where \mathbf{l} is a unit vector parallel to the disk angular momentum. The internal torque of the disk is represented by the complex variable G . We begin with Equations (37) and (38) in Lubow & Ogilvie (2000) that describe the evolution of a disk in the binary frame that rotates with angular velocity $\Omega_b = \Omega_b \mathbf{e}_z$. The equations are based on a linear theory that is valid for small warps and tilts. The equations are

$$\Sigma r^2 \Omega \left(\frac{\partial W}{\partial t} + i \Omega_b W \right) = \frac{1}{r} \frac{\partial G}{\partial r} - T i (W + W^*) \quad (6)$$

and

$$\frac{\partial G}{\partial t} + i \Omega_b G - \frac{T}{\Sigma r^2 \Omega} i G + \alpha \Omega G = \frac{\Sigma H^2 r^3 \Omega^3}{4} \frac{\partial W}{\partial r}, \quad (7)$$

where

$$T = \frac{GM_s}{4a_p^2} \left[b_{3/2}^{(1)} \left(\frac{r}{a_p} \right) \right] \Sigma r, \quad (8)$$

and $b_{3/2}^{(1)}$ is the Laplace coefficient.

We seek normal modes of the form l_x , l_y , G_x , and $G_y \propto e^{i\omega t}$ where ω is a complex eigenvalue. We can write

$$W = W_+ e^{i\omega t} + W_- e^{-i\omega^* t} \quad (9)$$

and

$$G = G_+ e^{i\omega t} + G_- e^{-i\omega^* t}, \quad (10)$$

where ω^* is the complex conjugate of the eigenvalue ω . We follow Lubow & Ogilvie (2000) and expand the equations in powers of the tidal potential such that

$$T = T^{(1)} + T^{(2)} + \dots, \quad (11)$$

$$W_+ = W_+^{(0)} + W_+^{(1)} + W_+^{(2)} + \dots, \quad (12)$$

$$W_- = W_-^{(1)} + W_-^{(2)} + \dots, \quad (13)$$

$$G_+ = G_+^{(1)} + G_+^{(2)} + \dots, \quad (14)$$

$$G_- = G_-^{(1)} + G_-^{(2)} + \dots, \quad (15)$$

and

$$\omega = \omega^{(0)} + \omega^{(1)} + \omega^{(2)} + \dots \quad (16)$$

To lowest order, the rigid tilt mode has

$$\omega^{(0)} = -\Omega_b \text{ and } W_+^{(0)} = \text{const.} \quad (17)$$

To first order Equations (6) and (7) become

$$i\omega^{(1)} \Sigma r^2 \Omega W_+^{(0)} = \frac{1}{r} \frac{dG_+^{(1)}}{dr} - iT^{(1)} W_+^{(0)}, \quad (18)$$

$$2i\Omega_b \Sigma r^2 \Omega W_-^{(1)} = \frac{1}{r} \frac{dG_-^{(1)}}{dr} - iT^{(1)} W_+^{(0)*}, \quad (19)$$

$$\alpha \Omega G_+^{(1)} = \frac{\Sigma H^2 r^3 \Omega^3}{4} \frac{dW_+^{(1)}}{dr}, \quad (20)$$

and

$$(2i\Omega_b + \alpha \Omega) G_-^{(1)} = \frac{\Sigma H^2 r^3 \Omega^3}{4} \frac{dW_-^{(1)}}{dr}. \quad (21)$$

The precession rate to first order can be found by integrating Equation (18) over the whole disk to find

$$\omega^{(1)} = - \frac{\int_{r_{\text{in}}}^{r_{\text{out}}} T^{(1)} W_+^{(0)} r \, dr}{\int_{r_{\text{in}}}^{r_{\text{out}}} \Sigma r^2 \Omega W_+^{(0)} r \, dr}. \quad (22)$$

We use the boundary conditions that the internal disk torque vanishes at the boundaries

$$G_{\pm}^{(1)}(r_{\text{in}}) = G_{\pm}^{(1)}(r_{\text{out}}) = 0. \quad (23)$$

We solve Equations (18) to (21) for a fixed surface density profile $\Sigma \propto r^{-3/2}$ and choose $W_+^{(0)} = 1$ to find $W_{\pm}^{(1)}$ and $G_{\pm}^{(1)}$. By considering the second-order terms, the change to the inclination of the disk is determined by the tilt growth rate

$$\mathcal{J}(\omega^{(2)}) = \frac{\int_{r_{\text{in}}}^{r_{\text{out}}} \left(\frac{4\alpha}{\Sigma H^2 r^4 \Omega^2} \right) (|G_+^{(1)}|^2 - |G_-^{(1)}|^2) r \, dr}{\int_{r_{\text{in}}}^{r_{\text{out}}} \Sigma r^2 \Omega |W_+^{(0)}|^2 r \, dr} \quad (24)$$

(Lubow & Ogilvie 2000). The sign of this determines whether the disk tilt increases or decreases. The $|G_+^{(1)}|$ term is caused by the $m = 0$ component of the potential and leads to damping while the $|G_-^{(1)}|$ term is caused by the $m = 2$ component and causes pure growth.

2.4. Tilt Growth Timescale

We calculate the tilt growth timescale as

$$\frac{t_{\text{growth}}}{P_{\text{orb}}} = \frac{\Omega_b}{2\pi |\mathcal{J}(\omega^{(2)})|}. \quad (25)$$

We consider a planet with a mass of $M_p = 10^{-3} M_s$. The disk extends from $r_{\text{in}} = 0.03 r_H$ up to r_{out} , which we vary. Note that because we parameterize the disk size in terms of the Hill sphere radius, the results presented are independent of the planet semimajor axis. The viscosity parameter is $\alpha = 0.01$. The left panel of Figure 1 shows a contour plot of the tilt growth timescale as a function of the disk outer radius and the disk aspect ratio. The darkest region shows the location of the primary resonance. The resonance is where the frequency of the lowest-order global bending mode in the disk matches the tidal forcing frequency, which is twice the binary orbital frequency ($2\Omega_b$). The trough becomes lower and narrower as α decreases (Lubow & Ogilvie 2000). Growth of the disk tilt occurs when the outer radius of the disk is close to the resonance. Even in the case of zero viscosity, disk tilt growth may occur if the disk is within the resonant band (Lubow & Ogilvie 2000). Note that larger disk aspect ratios correspond to larger viscous torques, for which we expect larger disks.

The white region shows where, for small H/r , the growth rate is positive, meaning that the disk tilt decays. The disk moves toward coplanar alignment with the orbital plane of the planet. However, for larger H/r , the growth rate is negative and the disk inclination increases. For a fixed disk outer radius, there is a narrow range of values for H/r for which the growth rate is very large.

Figure 2 shows a contour plot of the ratio of the growth timescale to the viscous timescale. The dark region shows where a disk is most unstable to the tilt instability. With a smaller α , the width of the unstable region is narrower (but at the same location) while the viscous timescale is longer. In this case, whether the disk can tilt depends sensitively upon the distribution of material within the disk. For larger α , the viscous timescale decreases and so while the disk is more unstable to tilting, there may not be sufficient time for it to occur.

3. Hydrodynamic Simulations

The analytic estimates assume a fixed power-law surface density and do not accurately model the truncation of the outer parts of the circumplanetary disk due to the tidal torques. To overcome these limitations we have investigated the tilt evolution using both smoothed particle hydrodynamics (SPH) and grid-based simulations.

3.1. SPH Simulations

We first use the SPH code PHANTOM (Lodato & Price 2010; Price & Federrath 2010; Price et al. 2018) to model a misaligned circumplanetary disk. PHANTOM has been used extensively to model misaligned disks in binary systems (e.g., Nixon et al. 2013; Franchini et al. 2019; Smallwood et al. 2019). The simulation has two sink particles, one representing the star with mass M_s and the other representing the planet with mass $M_p = 10^{-3} M_s$. The accretion radius of the star is $1.4 r_H$, while that of the planet is $0.03 r_H$. The simulation does not have

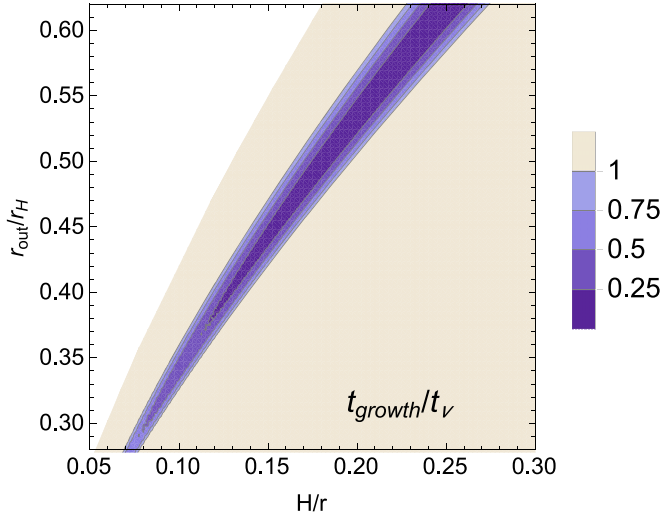


Figure 2. Contour plot of the ratio of the growth timescale of the tilt of a circumplanetary disk to the viscous timescale as a function of the disk aspect ratio H/r and the disk outer radius, r_{out} , in units of the Hill sphere radius. The planet mass is $M_p = 0.001 M_s$. The surface density is fixed as $\Sigma \propto r^{-3/2}$ distributed between $r_{\text{in}} = 0.03 r_H$ up to r_{out} . The disk viscosity is $\alpha = 0.01$. In the white region the disk tilt decreases. In the colored regions the disk tilt increases.

any dependence on the planet’s orbital separation since all lengths are scaled to the Hill radius. The planet is in a circular orbit. The disk is initially tilted to the binary orbital plane by 10° .

The surface density of the disk is initially distributed as a power law $\Sigma \propto r^{-3/2}$ between $r_{\text{in}} = 0.03 r_H$ up to $r_{\text{out}} = 0.4 r_H$. We note that the initial truncation radii of the disk do not significantly affect the evolution since the density evolves quickly. We have tested both smaller and larger initial outer truncation radii. The mass of the disk does not affect the evolution since we do not include disk self-gravity, and we take the initial total disk mass to be $10^{-6} M_s$. We consider three different initial SPH particle numbers, 250,000, 500,000, and 10^6 . The disk is locally isothermal with sound speed $c_s \propto r^{-3/4}$. This is chosen so that α and the smoothing length $\langle h \rangle/H$ are constant over the disk (Lodato & Pringle 2007). We take the aspect ratio at r_{in} to be $H/r = 0.2$. This corresponds to $H/r = 0.1$ at the initial outer truncation radius. We take the Shakura & Sunyaev (1973) α parameter to be 0.01. This is the lowest value that can be physically resolved in SPH simulations at the lowest resolution we employed (Price et al. 2018). We implement the disk viscosity by adapting the SPH artificial viscosity according to the procedure described in Lodato & Price (2010) with $\alpha_{\text{AV}} = 0.36, 0.46, 0.58$, in order of increasing resolution, and $\beta_{\text{AV}} = 2$. The circumplanetary disk is initially resolved with shell-averaged smoothing length per scale height $\langle h \rangle/H = 0.28, 0.22$, and 0.17 in order of increasing resolution.

Figure 3 shows the inclination and nodal precession angle for the circumplanetary disk. The disk nodally precesses at roughly a constant rate as a result of the $m = 0$ tidal torque component. There are small-scale oscillations on a timescale $P_{\text{orb}}/2$ as a result of the $m = 2$ tidal torque component. The inclination of the disk increases in time meaning that the dissipation of the $m = 2$ component dominates. This is in agreement with the analytic predictions in the previous section that circumplanetary disks are unstable to tilting. We have also run simulations with

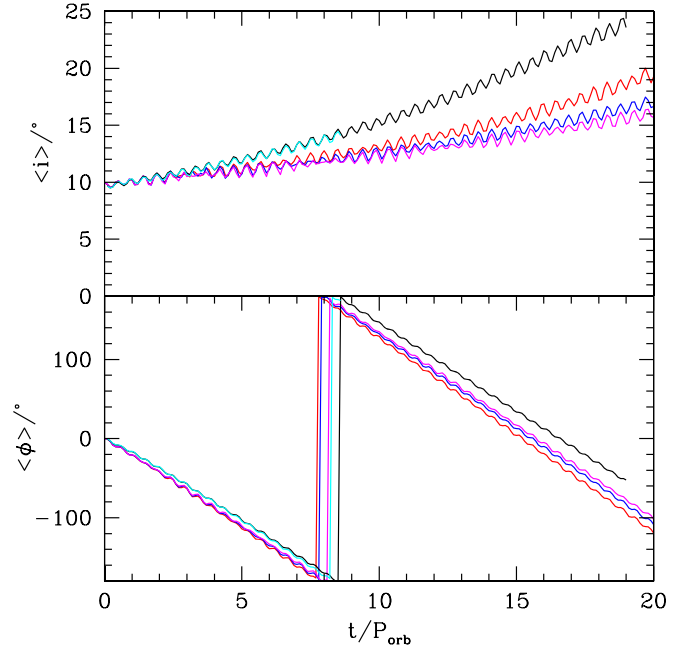


Figure 3. Hydrodynamic simulations of a circumplanetary disk that is initially misaligned by 10° showing the inclination of the disk (upper panel) and the nodal precession angle (lower panel). The angles are averaged by mass over the radial extent of the disk. The SPH simulations have 250,000 particles (red), 500,000 particles (blue), and 10^6 particles (magenta) initially. The grid simulation results are shown as the black (low-resolution) and cyan (high-resolution) curves. The SPH and grid simulations both have an outer aspect ratio of $H/r = 0.1$, though they differ in details of the initial disk profile.

varying disk aspect ratio and find that growth occurs for $H/r \gtrsim 0.05$.

3.2. Grid Simulations

We have carried out independent grid-based simulations with ATHENA++ (Stone et al. 2020), using a planet-centered spherical-polar coordinate system. The simulation domain extends from $0.0286 r_H$ to r_H in the radial direction, from 0.2 to $\pi - 0.2$ in the θ direction, and a full 2π in the ϕ direction. One level of mesh refinement is applied at $\theta = [0.885, 2.256]$. The third-order reconstruction scheme has been adopted. The circumplanetary disk’s density and temperature profiles are the same as the SPH simulations in Section 3.1. The disk surface density has an exponential tail of $\exp(-(r/r_{\text{cut}})^2)$ with $r_{\text{cut}} = 0.3 r_H$. The detailed disk and grid setup is presented in Zhu (2019). Two simulations with different resolutions have been carried out. In the low-resolution run, we have $72 \times 56 \times 128$ grids at the base level in the $r \times \theta \times \phi$ domain. With one level of mesh refinement, this is equivalent to 8 grid cells per scale height at the inner boundary and 5 grid cells per scale height at r_{cut} . Based on Zhu (2019), this is the minimum resolution required to study disk precession. To verify convergence, we have doubled the resolution in every direction and carried out a high-resolution simulation. Due to the computational cost, we have only run the high-resolution simulation for $\sim 9 P_{\text{orb}}$.

Figure 3 shows the evolution of tilt in the grid-based simulations. The high-resolution run is almost identical to the low-resolution run, and displays similar but somewhat faster tilt growth than the corresponding SPH simulations. Figure 4 shows the disk’s isodensity contours at 3 and $19 P_{\text{orb}}$ from the low-resolution simulation. Clear growth of the disk inclination

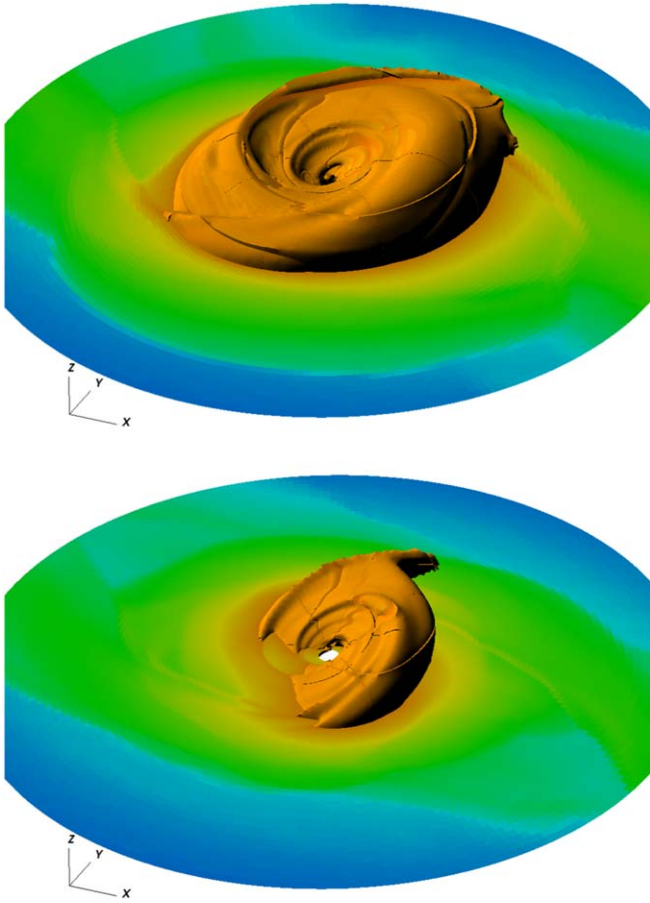


Figure 4. The disk’s isodensity contours for the ATHENA++ low-resolution run at $3 P_{\text{orb}}$ (the upper panel) and $19 P_{\text{orb}}$ (the lower panel). The disk has the same nodal precession angle at these two snapshots.

is observed at $19 P_{\text{orb}}$. We can also see that the disk is significantly depleted with time due to accretion.

4. Discussion and Conclusions

Fluid disks in binary systems can be linearly unstable to the growth of disk tilt (Lubow 1992). In this Letter we have argued that the physical conditions of circumplanetary disks—their aspect ratios and outer truncation radii—are favorable for rapid tilt growth, at least in the limit where the disks are detached and not accretion dominated. Fast tilt growth is predicted analytically, and recovered in SPH and grid-based simulations that include physical effects (such as tidal truncation and spiral waves) that are not readily modeled analytically. We have not included the effect of accretion from the circumstellar disk on to the circumplanetary disk, which we expect to act as an effective damping term. Nonetheless, given the rapid growth rates that we have found for $H/r \gtrsim 0.05$, we expect there to be a regime of parameter space for which circumplanetary disks commonly exhibit substantial tilts. If correct, there will be implications both for the observability of circumplanetary disks, and for the properties and dynamics of satellite formation within them.

We have assumed that the planet is spherical in this work. The oblateness of a spinning planet would act to align the inner parts of the circumplanetary disk to the spin of the planet. In the classical scenario, where the disk at large radius aligns to the orbital plane while the planet obliquity may be nonzero, the

result is a warped nonprecessing disk whose shape follows the Laplace surface (Tremaine et al. 2009). In the presence of tilt instability, the outer part of the disk will be misaligned and precess on a relatively short timescale. Although the torque that a warped disk exerts on the planet shortens the timescale on which the planet spin-axis changes (compared to the accretion-only limit, see, e.g., the analogous black hole situation; Scheuer & Feiler 1996), the precession is likely to limit obliquity evolution. The combined effects of a warp and outer disk precession might restrict where in the disk regular satellites are able to form.

In future work we plan to investigate a range of circumplanetary disk parameters and study the long-term behavior of disks that exhibit tilt instability. We expect sufficiently high inclinations to trigger the onset of Kozai–Lidov (Kozai 1962; Lidov 1962) oscillations, which exchange inclination and eccentricity of the disk (Martin et al. 2014; Fu et al. 2015). The critical inclination for a disk to become Kozai–Lidov unstable depends upon the disk aspect ratio (Lubow & Ogilvie 2017; Zanazzi & Lai 2017). We also note that while a circumplanetary gas disk may be stable against Kozai–Lidov oscillations, any solid bodies that form within the gas disk may become unstable once the gas disk has dissipated (e.g., Speedie & Zanazzi 2019).

We thank Daniel Price for providing the PHANTOM code for SPH simulations. Computer support was provided by UNLV’s National Supercomputing Center. ATHENA++ simulations were carried out at the Texas Advanced Computing Center (TACC) at The University of Texas at Austin through XSEDE grant TG-AST130002, and using resources from the NASA High-End Computing (HEC) Program through the NASA Advanced Supercomputing (NAS) Division at Ames Research Center. We acknowledge support from NASA TCAN award 80NSSC19K0639. Z.Z. acknowledges support from the National Science Foundation under CAREER Grant Number AST-1753168.

ORCID iDs

Rebecca G. Martin <https://orcid.org/0000-0003-2401-7168>
 Zhaohuan Zhu <https://orcid.org/0000-0003-3616-6822>
 Philip J. Armitage <https://orcid.org/0000-0001-5032-1396>

References

- Akinsanmi, B., Santos, N. C., Faria, J. P., et al. 2020, *A&A*, **635**, L8
- Artymowicz, P., & Lubow, S. H. 1996, *ApJL*, **467**, L77
- Ayliffe, B. A., & Bate, M. R. 2009a, *MNRAS*, **393**, 49
- Ayliffe, B. A., & Bate, M. R. 2009b, *MNRAS*, **397**, 657
- Bate, M. R., Bonnell, I. A., & Bromm, V. 2003, *MNRAS*, **339**, 577
- Bate, M. R., Bonnell, I. A., Clarke, C. J., et al. 2000, *MNRAS*, **317**, 773
- Batygin, K., & Morbidelli, A. 2020, *ApJ*, **894**, 143
- Benz, W., Slattery, W. L., & Cameron, A. G. W. 1989, *Metic*, **24**, 251
- Brasser, R., & Lee, M. H. 2015, *AJ*, **150**, 157
- Canup, R. M., & Ward, W. R. 2002, *AJ*, **124**, 3404
- D’Angelo, G., Henning, T., & Kley, W. 2002, *A&A*, **385**, 647
- Franchini, A., Martin, R. G., & Lubow, S. H. 2019, *MNRAS*, **485**, 315
- Fu, W., Lubow, S. H., & Martin, R. G. 2015, *ApJ*, **807**, 75
- Gressel, O., Nelson, R. P., Turner, N. J., & Ziegler, U. 2013, *ApJ*, **779**, 59
- Jontof-Hutter, D., Lissauer, J. J., Rowe, J. F., & Fabrycky, D. C. 2014, *ApJ*, **785**, 15
- Katz, J. I., Anderson, S. F., Margon, B., & Grandi, S. A. 1982, *ApJ*, **260**, 780
- Kozai, Y. 1962, *AJ*, **67**, 591
- Larwood, J. D., Nelson, R. P., Papaloizou, J. C. B., & Terquem, C. 1996, *MNRAS*, **282**, 597
- Lidov, M. L. 1962, *P&SS*, **9**, 719

- Lin, D. N. C., & Papaloizou, J. 1986, [ApJ](#), **309**, 846
- Lodato, G., & Price, D. J. 2010, [MNRAS](#), **405**, 1212
- Lodato, G., & Pringle, J. E. 2007, [MNRAS](#), **381**, 1287
- Lubow, S. H. 1992, [ApJ](#), **398**, 525
- Lubow, S. H., Martin, R. G., & Nixon, C. 2015, [ApJ](#), **800**, 96
- Lubow, S. H., & Ogilvie, G. I. 2000, [ApJ](#), **538**, 326
- Lubow, S. H., & Ogilvie, G. I. 2017, [MNRAS](#), **469**, 4292
- Lubow, S. H., Seibert, M., & Artymowicz, P. 1999, [ApJ](#), **526**, 1001
- Lunine, J. I., & Stevenson, D. J. 1982, [Icar](#), **52**, 14
- Martin, R. G., & Lubow, S. H. 2011, [MNRAS](#), **413**, 1447
- Martin, R. G., Nixon, C., Lubow, S. H., et al. 2014, [ApJL](#), **792**, L33
- Masuda, K. 2014, [ApJ](#), **783**, 53
- Millholland, S., & Batygin, K. 2019, [ApJ](#), **876**, 119
- Miranda, R., & Lai, D. 2015, [MNRAS](#), **452**, 2396
- Morbidelli, A., Tsiganis, K., Batygin, K., Crida, A., & Gomes, R. 2012, [Icar](#), **219**, 737
- Mosqueira, I., & Estrada, P. R. 2003, [Icar](#), **163**, 198
- Nixon, C., King, A., & Price, D. 2013, [MNRAS](#), **434**, 1946
- Paczynski, B. 1977, [ApJ](#), **216**, 822
- Papaloizou, J. C. B., & Terquem, C. 1995, [MNRAS](#), **274**, 987
- Piro, A. L., & Vissapragada, S. 2020, [AJ](#), **159**, 131
- Price, D. J., & Federrath, C. 2010, [MNRAS](#), **406**, 1659
- Price, D. J., Wurster, J., Tricco, T. S., et al. 2018, [PASA](#), **35**, e031
- Pringle, J. E. 1981, [ARA&A](#), **19**, 137
- Rogoszinski, Z., & Hamilton, D. P. 2020, [ApJ](#), **888**, 60
- Safronov, V. S. 1966, [SvA](#), **9**, 987
- Scheuer, P. A. G., & Feiler, R. 1996, [MNRAS](#), **282**, 291
- Schulik, M., Johansen, A., Bitsch, B., Lega, E., & Lambrechts, M. 2020, [arXiv:2003.13398](#)
- Shakura, N. I., & Sunyaev, R. A. 1973, [A&A](#), **24**, 337
- Smallwood, J. L., Lubow, S. H., Franchini, A., & Martin, R. G. 2019, [MNRAS](#), **486**, 2919
- Speedie, J., & Zanazzi, J. J. 2019, [arXiv:1912.00034](#)
- Stone, J. M., Tomida, K., White, C. J., & Felker, K. G. 2020, [ApJS](#), **249**, 4
- Szulágyi, J., Morbidelli, A., Crida, A., & Masset, F. 2014, [ApJ](#), **782**, 65
- Tanigawa, T., Ohtsuki, K., & Machida, M. N. 2012, [ApJ](#), **747**, 47
- Terquem, C. E. J. M. L. J. 1998, [ApJ](#), **509**, 819
- Tremaine, S., Touma, J., & Namouni, F. 2009, [AJ](#), **137**, 3706
- Vokrouhlický, D., & Nesvorný, D. 2015, [ApJ](#), **806**, 143
- Ward, W. R., & Hamilton, D. P. 2004, [AJ](#), **128**, 2501
- Zanazzi, J. J., & Lai, D. 2017, [MNRAS](#), **467**, 1957
- Zhu, Z. 2015, [ApJ](#), **799**, 16
- Zhu, Z. 2019, [MNRAS](#), **483**, 4221